Savanna model - report

ABSTRACT

In this work, first the Staver-Levin [4] Savanna model was investigated in the framework of **C**hemical **M**aster **E**quation (CME) and then model parameters were tuned in order to fit the actual data from MODIS satellite observations [5]. It will be eventually shown that the CME algorithm lends itself to better fit the experimental data in ways which are not accessible to a standard ODE analysis. Results will suggest that CME method is able to interpret and reproduce the bistable behaviour which is instead difficult to be described with traditional approach for the analysis of dynamical systems.

ODE and CME results will be compared with experimental data in the conclusions and the most crucial features of the CME approach will be discussed. The obtained results suggest that the CME approach can indeed be regarded as more suitable than a traditional ODE analysis for modelling a dynamical system with such a complex phase space and large amount of parameters.

Contents

Part I

Savanna model

1 Savanna biome and satellite data

1.1 Grass-savanna sapling-forest model

Several models are present in literature which attempt to describe specific features of the interactions between grass, savanna saplings and trees. The underlying common feature for those models is to consider the time evolution of a three states *population* of *Forest trees* (**F**), *Savanna saplings* (**S**) and *Grass* (**G**) and taking into account their hierarchical competition due to the different biological features of each one. The most crucial part in the modelling process consist of making hypothesis on the inter-dependency of the G, S and T as shown in [2].

1.2 Satellite observations

Models are generally used to study the sub-saharan region ($\in [35^oS - 15^oN]$), with little to none anthropic activities and far from water sources in order to ignore areas in which other variables (anthropogenic and natural ones) have non-negligible contributions.

The main probe for investigate qualitative features and collect data for quantitative analysis are satellite observations in visible and far-IR range. In particular, for the purpose of this work, data used in [5] from MODIS[1] satellite have been used.
Please note that the MODIS observations cannot tell saplings ($< 5m$ height) from grasses and therefore it is more suitable to split satellite data in tree/non-tree coverage per pixel observed. Experimental *non-tree coverage* MODIS data will therefore be compared with the grasses (rather than grasses *and* saplings) in simulations.

[1] `https://modis.gsfc.nasa.gov/`

Principal Component Analysis Cleaned up data from MODIS are represented in Fig.1. On top of that, it is meaningful to arrange data according to the **M**ean **A**nnual **R**ainfall so that the largest variance can be observed, as shown from a preliminary **P**rincipal **C**omponent **A**nalysis[2] (PCA) in Fig.2. For the purpose of this investigation, only entries

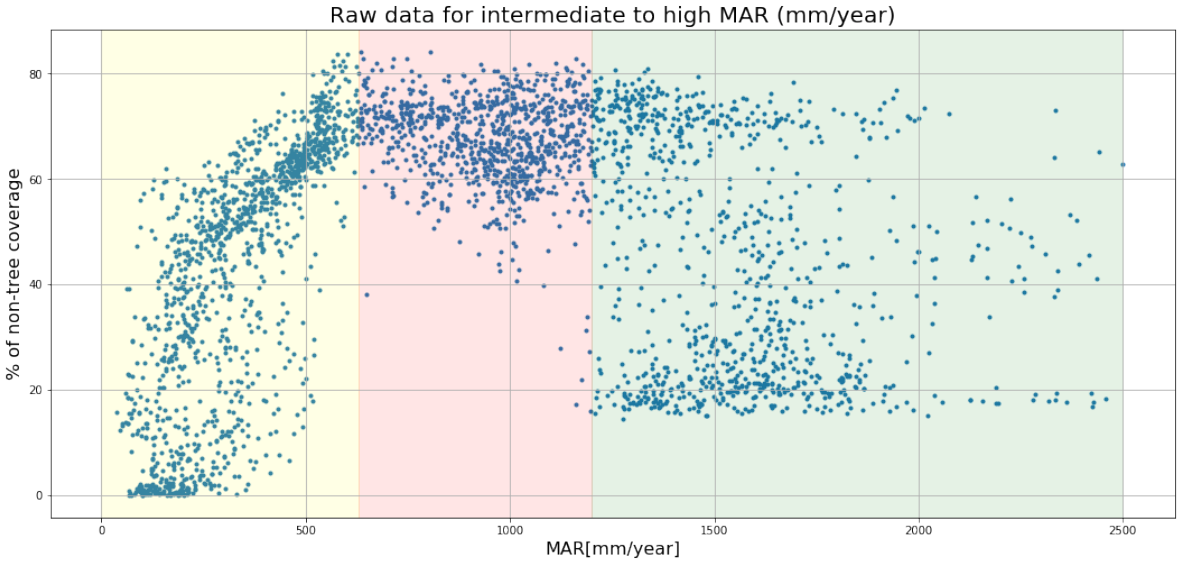

Figure 1: From [5]. The three highlighted regions corresponds to the three different regimes of MAR, $R1 \in [0, 630]$ (yellow), $R2 \in [630, 1200]$ (red), $R3 \in [1200, 2500]$ (green).

in $R2 + R3$ MAR regimes are going to be considered. This choice will be justified in Sec.2 where the *Savanna model* will be introduced..
As it is possible to infer from Fig.1, due to MODIS artifacts, data in $R2 + R3$ regimes range between 20% and 80%: for an easier comparison with the results from the simulations, data entries in $R2 + R3$ will be scaled in order to fit the $0\% - 100\%$ range and a scaled expression for the MAR in the $R2 + R3$ regime (r in Fig.9) will be used.

[2]Note that PCA is based on linear transformations only and therefore it cannot properly perform dimensionality reduction on data which lies on non-linear manifold [6]. However, as the two main directions obtained from PCA components were indeed representative of the crucial parameters which are generally investigated in literature, no further exploration in dimensionality reduction was performed and data will be analyzed in terms of non-tree coverage as a function of MAR.

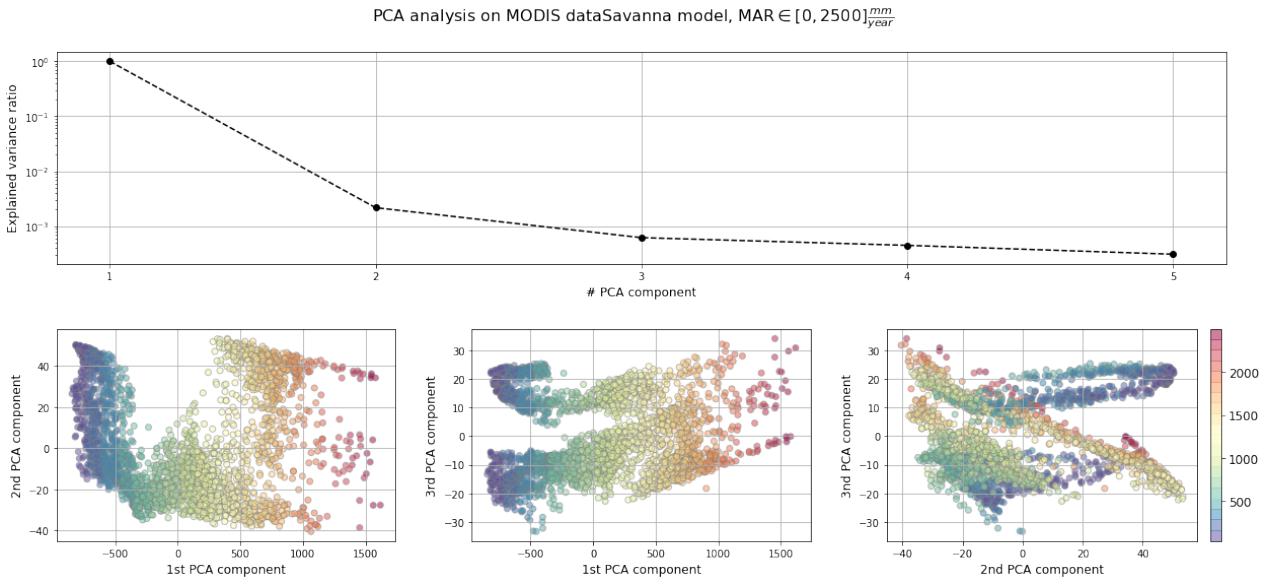

Figure 2: PCA from data in Fig.1.It is easy to point out that the first two PCA components are mostly representative respectively of the MAR and the non-tree coverage in Fig.1. Moreover, the explained variance ratio in the top plot suggests that the first two PCA components are already sufficient to represent the data and that the maximum variance is along the first PCA component axis. Colors are used to refer to the correspondent MAR for each entry in the reduced PCA space.

2 Mean-field Staver-Levin model

For the purpose of this work, Staver model [3] will be studied. This model (Eq.1) is based on the assumption that a *mean field* approach can be used for studying the interactions between trees, saplings and grasses in the savanna model. This fundamental hypothesis can be considered valid as data from MODIS are sampled with a pixel linear size resolution

Variable	Symbol
% of grass states	g
Total number of grass states	G
% of saplings states	s
Total number of saplings states	S
% of tree states	t
Total number of tree states	T
Saplings mortality rate	μ
Tree mortality rate	ν
Saplings birth rate	β
Saplings to tree coefficient	ω
Jacobian matrix	J

Table 1: Notation used, based on [3].

of about $50km$, way larger than the typical sizes of each individual grass, sapling or tree unit.

$$\begin{cases} \dot{g} = \mu s + \nu t - \beta g t \\ \dot{s} = \beta g t - (\omega(g) + \mu) s \\ \dot{t} = \omega(g) s - \nu t \end{cases} \tag{1}$$

With the meaning of each parameter given in Tab.1. Note that in this model, it is assumed that only g affects the magnitude of the *sapling-to-tree* growth coefficient. Even if in [3] a sigmoid function was used for the $\omega(G)$ expression so that $\omega(g) = \omega_0 + \frac{\omega_1 - \omega_0}{1 + e^{-\frac{(g-\theta_1)}{s_1}}}$, it was experimented that an hyperbolic tangent function yielded better results for this benchmark case and therefore the expression in Eq.2 was used later on.

$$\omega(g) = \omega_0 + (\omega_1 - \omega_0) \cdot \tanh(\frac{g - \theta_1}{s_1}) \tag{2}$$

Eq.2 still preserved the most crucial features for the model (namely it works as an"activation function" for $\omega(g)$), still with constant values at high and low MAR regimes, but a faster transition between these two regimes. A comparison between the two can be observed in Fig.3.

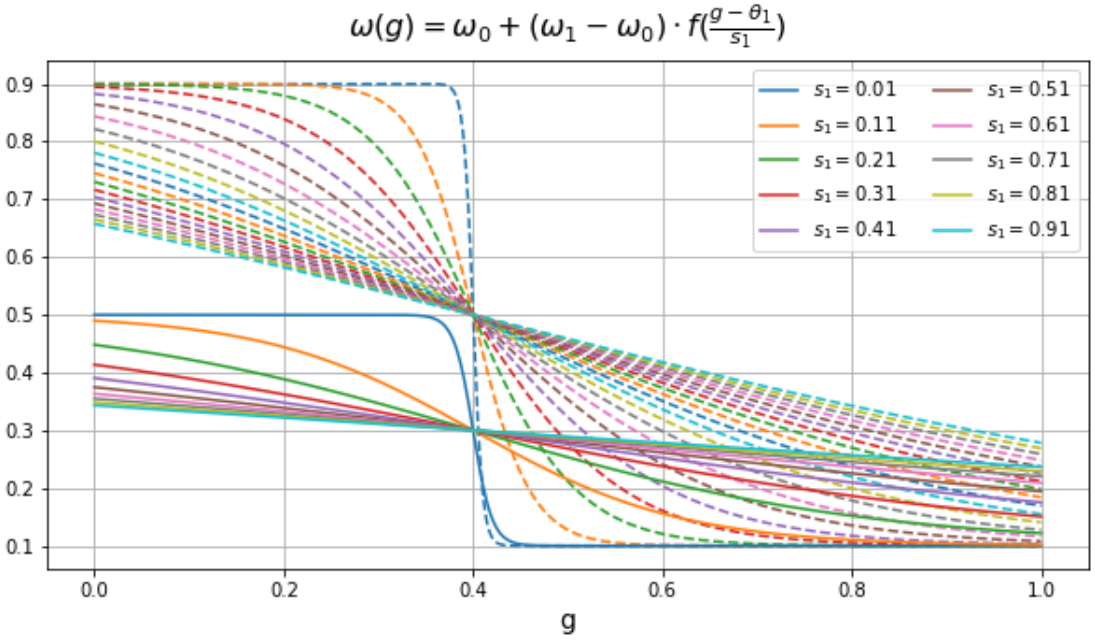

Figure 3: Comparison of the $\omega(G)$ functions for different s_1 parameters for $\omega_0 = .9$, $\omega_1 = .4$, $\theta_1 = .4$ (parameters from [3]). Solid lines: $f = sigmoid$ from Staver model; Dashed lines: $f = tanh$ expression from this work.

A fundamental hypothesis that will be used in this analysis is that the there is a finite maximum coverage for the system of `N` states so that the $g + t + s = 1$. Therefore, using

the $g + s + t = 1$ boundary condition, it is possible to consider one of the equations Eq.1 redundant: this means that the 3D ODE system in Eq.1 can be studied w.l.o.g. as a 2D model:

$$\begin{cases} \dot{g} = \mu(1 - g - t) + \nu t - \beta g t \\ \dot{t} = \omega(g)(1 - g - t) - \nu t \end{cases} \tag{3}$$

2.1 Analytical analysis of dynamical system

Even if an expression for ω_G different from the one in literature has been used, still it is possible to analytically investigate the stability of the system in Eq.3.

$$\boldsymbol{J_{2D}} = \begin{pmatrix} \frac{\partial \dot{g}}{\partial g} & \frac{\partial \dot{g}}{\partial t} \\ \frac{\partial \dot{t}}{\partial g} & \frac{\partial \dot{t}}{\partial t} \end{pmatrix} = \begin{pmatrix} -\mu - \beta t & -\mu + \nu - \beta g \\ \frac{d\omega(g)}{dg}(1 - g - t) - \omega(g) & -\omega(g) - \nu \end{pmatrix} \tag{4}$$

Solving the eigenvalues and eigenvectors of Eq.4 allows for an identification and classification, for given rainfall regimes and model parameters critical points of the dynamical system in Eq.3.

Transcritical bifurcation It can be verified that, if $g = 1$, $Tr[\mathbf{J_{2D}}]$ is always negative while $Det[\mathbf{J_{2D}}]$ is positive for $\beta\omega_1 < (\omega_1 + \mu)\nu$. In this case, a zero and a negative eigenvalue results from $\mathbf{J_{2D}}$. This suggests that the system in $g = 1$ undergoes a transcritical bifurcation where β changes sign, from stable equilibrium if $\beta < \frac{(\omega_1+\mu)\nu}{\nu\omega_1}$ to unstable if $\beta > \frac{(\omega_1+\mu)\nu}{\nu\omega_1}$.

Stability and bistability For the general case of $g < 1$, $Tr[\mathbf{J_{2D}}]$ is always less then zero and therefore the equilibrium of the system is fully characterized from the sign of $Det[\mathbf{J_{2D}}]$. It has been proved [3] that an expansion to $\mathcal{O}(g)$ for the $Det[\mathbf{J_{2D}}]$ expression can be used to justify the presence of bistability of the system.
Following the same dynamical system equations from Staver[4], the very same result can be proven using **R**outh–**H**urwitz (RH) criterion for stability: if the two following conditions are met

- $Tr[\mathrm{J}] < 0$
- $Det[\mathrm{J}] > 0$

the eigenvalues of J have negative real part while the zero eigenvalues is representative of the existence of an absorbing state for the system. It is easy to see that the condition on $Tr[J]$ is always met while the condition on the $Det[\mathrm{J}]$ is verified provided that it exists a $g*$ such that:

$$\frac{d\omega(g^*)}{dg} > -\frac{\beta\mu\nu}{(\beta g^* - \nu)^2} = \frac{df(g^*)}{dg} \tag{5}$$

with the $\omega(g^*)$ now equal to

$$\omega(g^*) = \frac{\beta\nu}{\beta g^* - \nu} \tag{6}$$

and it is possible to characterize easily the equilibria of the dynamical system as qualitatively shown in Fig.4, provided that the $\omega(G)$ has a sigmoid-like shape.

Note that, as no explicit assumption was made on the $\omega(g)$ function, still the same theoretical framework in [4] can be used to investigate the stability of this system. In the preliminary simulations for the Savanna model, when the parameters were all considered as constant, the eigenvalues of the Jacobian matrix were evaluated for different size `N` of the system and different parameters. An example of this analysis can be seen in Fig.5 and Fig.6: apart for the first eigenvalue always being zero (corresponding to the absorbing state), the analysis of the second eigenvalue for different size of the system and different β allowed to infer how rapidly the system was attracted to the equilibrium configuration depending on (`N`,β). However, as in the following sections the simulations are performed using variable parameters depending on the MAR, this analysis will not be systematically reproduced.

2.2 Beyond standard ODE approach

Fig.7 shows ODE solutions of Staver model in [3] for few different initial conditions: this preliminary analysis suggests that the model in Eq.3 shows bistable and transcritical phase transitions which are strongly dependent on the initial conditions *and* on the parameters chosen for the system as shown in [3].

Limitation in ODE analysis Note also that, as the ODE solution represents a *point-to-point* correspondence between an initial state and its corresponding final state, no hint of bistability nor bistability ranges can be inferred unless the phase space is sampled with high enough resolution. Another typical issue of applying ODE analysis to such and similar models is that bistability related phenomena as flickering between stable states cannot be simulated and, consequently, it is inappropriate sometimes to relate ODE analytical models to real case scenarios.
This trait in particular motivated a further analysis using different kind of algorithms for evaluating the time evolution of distributions of **P**robability **D**ensity **F**unctions (PDF) in the phase space and in order to be able to pinpoint and characterize peculiar (e.g. bistable) regions of the phase space for a given system. In the next section, unique features of the CME approach in place of the traditional study of the point-to-point correspondence from the ODE will be presented, thus supporting the idea that such a methodology is more suitable for such an similar scenarios.

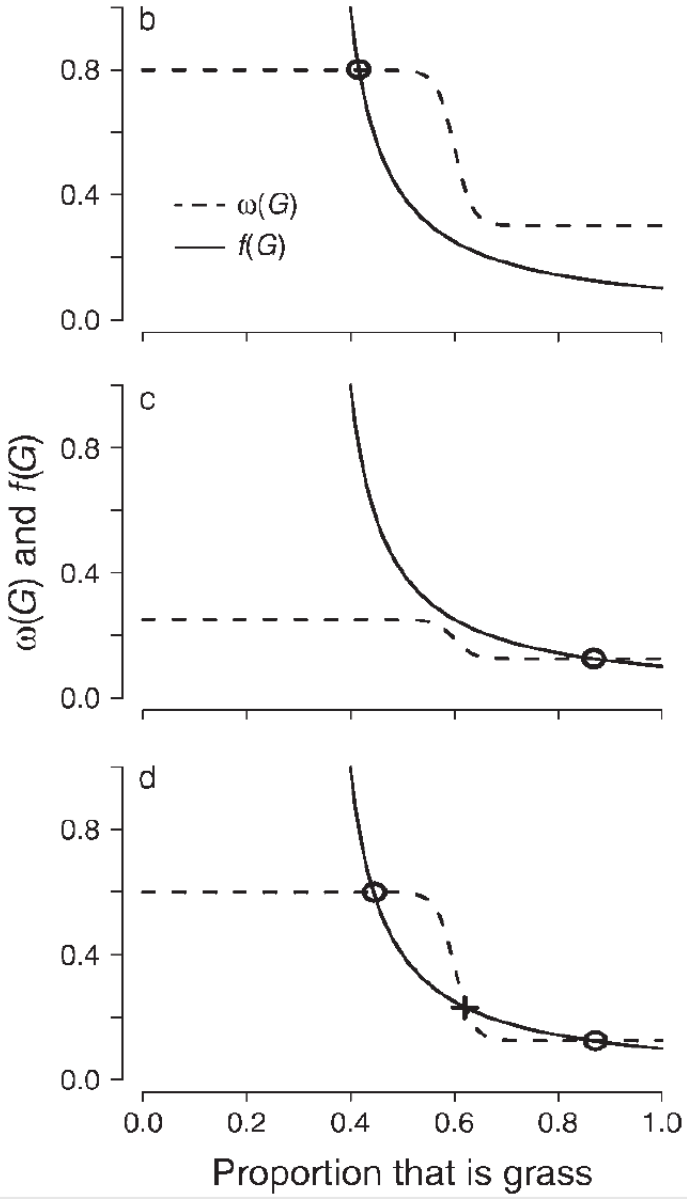

Figure 4: From [4]: Equilibrium landscape for the Staver savanna model. Open ovals are representative of stable equilibria, "+" represent unstable equilibrium. Depending on the parameters of the model, there could be: (b) a stable lowgrass equilibrium, (c) a stable high-grass equilibrium, and (d) stable high- and low-grass equilibria.

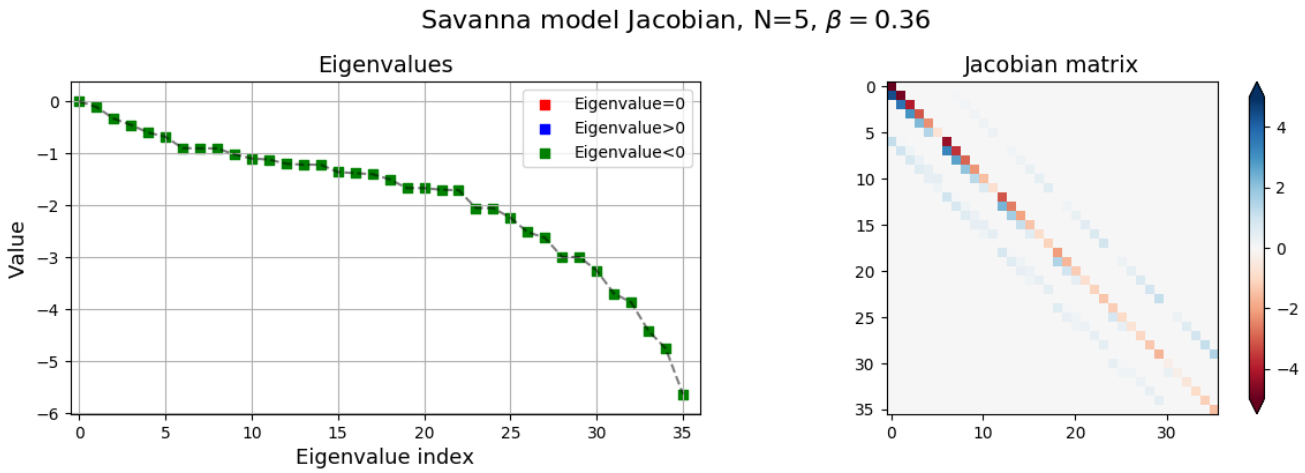

Figure 5: An example of the magnitude of the second eigenvalues for a low size system at $\beta = .36$ following the Staver model in [3] with the same (fixed) parameters as the one in this reference.

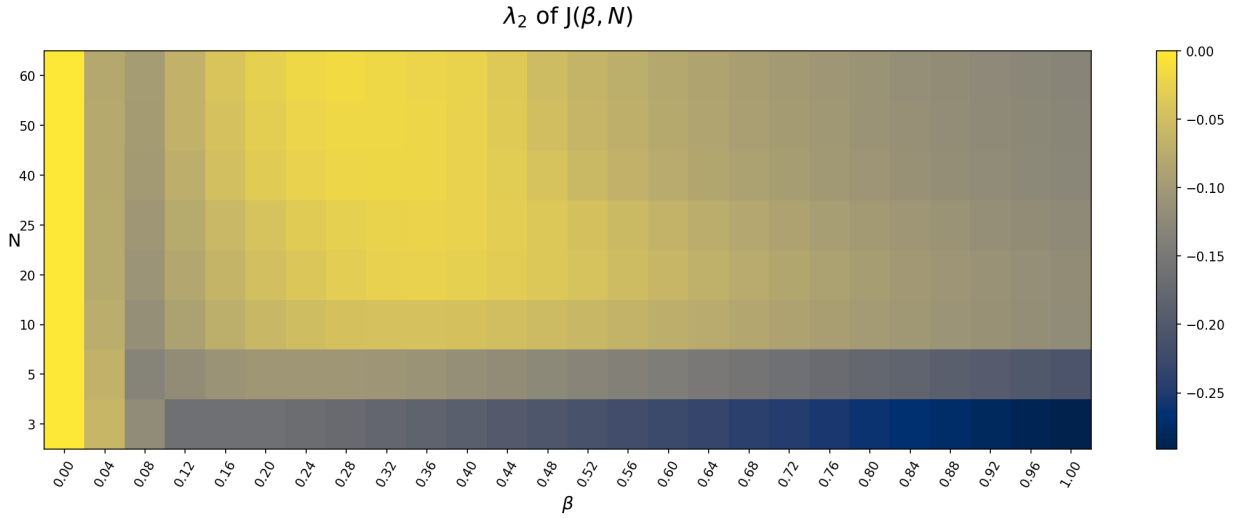

Figure 6: Example of heatmap of second eigenvalue λ_2 of J for different N and β-s for constant parameters from [3].

3 Chemical Master Equation for Savanna model

Chemical **M**aster **E**quation (CME) algorithm stems from considerations of *chemical* reactions between components in the system, limited by the **B**oundary **C**onditions (BC) on the system (e.g. its size, number of reactant needed for a given reaction to take place,...)[1]. Note that the *mean-field* approach used in Staver model matches the CME algorithm underlying hypothesis to consider a stirred system in which the reactants are diluted throughout the system.
The CME can be used for determining the time evolution of a system by paraphrasing its

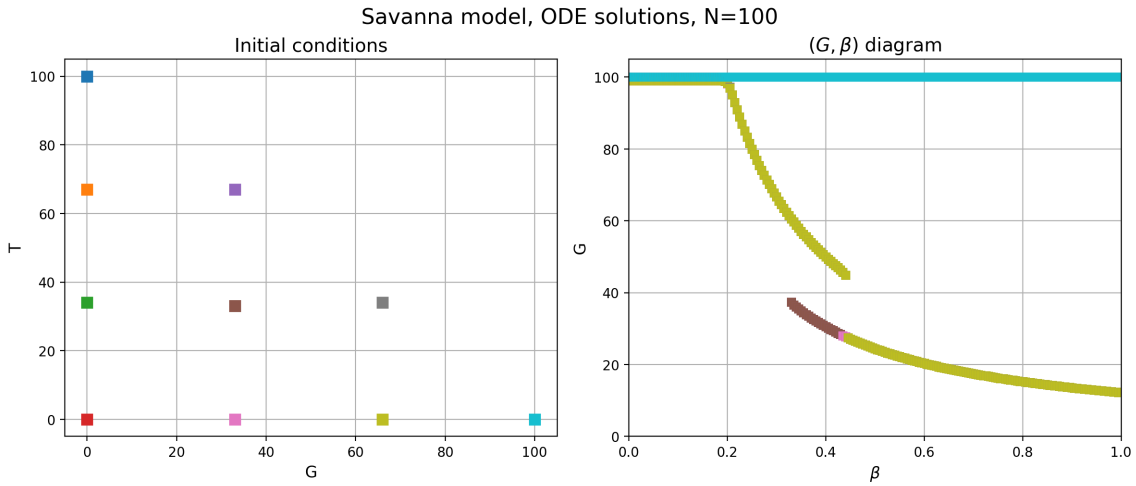

Figure 7: Bifurcation analysis of the dynamical system in Eq.3 as a function of G and β for constant parameters in [3]. Correspondent colors are representative of the same initial conditions. Note (e.g.) the analytical case of $G = N$ corresponding to an unstable equilibrium.

given ODE model in terms of possible *reactions* that can occur, starting from their average probability in a fully deterministic way. For this case of study, starting from Eq.3, it is possible to use the $g + s + t = 1$ BC so that the possible reactions that can occur in the system boils down to a fully deterministic set of four possible reactions:

$$\mathbf{R_1} \quad (G,T) \overset{\mu(N-G-T)}{\Longrightarrow} (G+1,T), \qquad \forall G \neq N$$

$$\mathbf{R_2} \quad (G,T) \overset{\nu T}{\Longrightarrow} (G+1,T-1), \qquad \forall G \neq N \text{ and } \forall T \neq 0$$

$$\mathbf{R_3} \quad (G,T) \overset{\frac{\beta}{N}GT}{\Longrightarrow} (G-1,T), \qquad \forall G \neq 0$$

$$\mathbf{R_4} \quad (G,T) \overset{\omega(G)(N-G-T)}{\Longrightarrow} (G,T+1), \qquad \forall T \neq N$$

These reactions can be arranged together in a matrix form in order to represent the Jacobian matrix for the time evolution of a given initial state, as shown in List.1. This means that, starting from an array $\mathbf{X}$ of states, and given a Jacobian matrix $\mathtt{J}$, the time evolution of the system can be obtained by integrating over time $\mathtt{J} \cdot \mathbf{X}$ [3].

[3] It is relevant to point out that a characteristic downside of CME algorithm is that introducing a new dimension in the system dramatically affects the dimension of the phase space: this results in working with dimension ≥ 2 having rapidly increasing computational costs when an higher resolution is needed. However, for the purpose of this work, a full simulation could still be easily performed on a common laptop in a few hours.

3.1 CME approach

Several preliminary tests have been made on systems of different N-s and a size of N= 50 turned out to be a good compromise between sufficient resolution and reasonable enough computational times. However, it is a peculiar feature of the CME to be able to effectively reproduce the dynamical behaviour of systems having low size (in the order of a few units) still well within the underlying hypotheses for this algorithm. Nevertheless, for the purpose of comparison with experimental data, this case was not investigated for the Savanna model.
In this work, a symmetric gaussian distribution PDF in the 2D phase space with dispersion equal to $\frac{N}{10}$ and different mean positions will be considered as initial conditions. It was shown in tests of CME algorithm on other models (bistable toggle switch, SIS, SIR) that the spread of initial conditions affects the final distribution of the PDF especially when bistable regions are present in the phase space.
An additional crucial feature of CME approach when compared to a classic ODE study of the model is that, as in CME PDF are investigated, CME algorithms are more suitable to study experimental scenarios in which there is an intrinsic indeterminacy over the initial state of the system due (e.g.) to resolution of probing instruments which thus can be easily represented in terms of dispersion of the initial conditions.

3.2 β and ν dependency on MAR

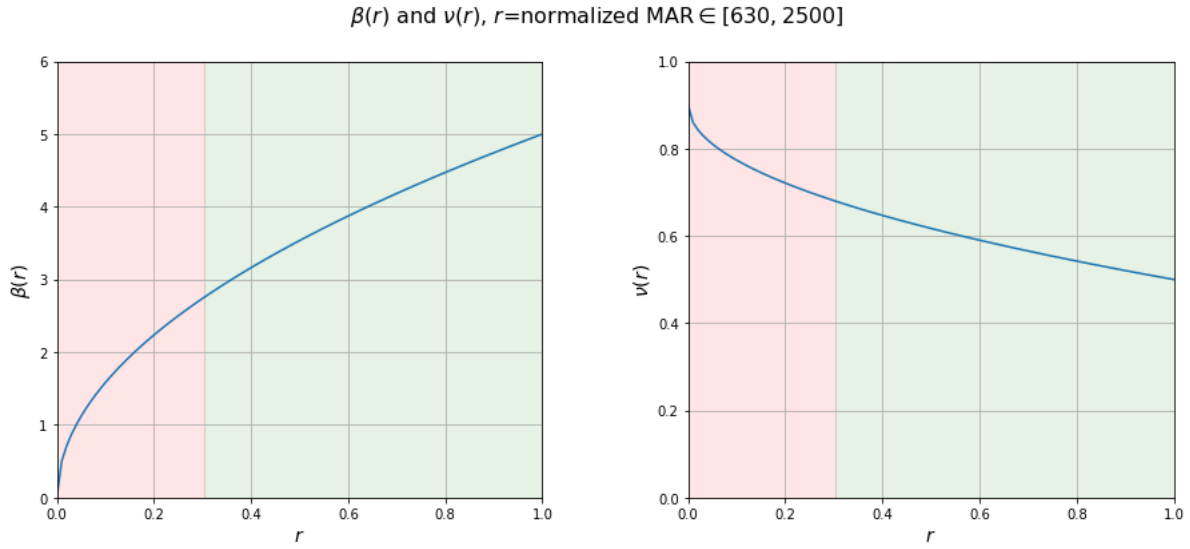

Figure 8: Examples of $\beta(r) = \beta_0 + (\beta_1 - \beta_0)\sqrt{r}$ and $\nu(r) = \nu_0 - (\nu_1 - \nu_0)\sqrt{r}$ functions used in the following simulations. As in previous plots, red and green regions represent respectively R2 and R3 rainfall regimes.

As it has been chosen a representation of the data as a function of the rainfall, it has been suggested to more appropriately account for dependencies of the parameters of the model

on r. In particular, it has been pointed out that, in $R2 + R3$ rainfall regimes, the parameters that are most likely to be dependent on rainfall are the sapling birth rate β and the tree mortality rate ν while it has been assumed that all the other parameters can be considered constant.

In a first stance, a simple linear (increasing for β, decreasing for ν) dependency on the rainfall was assumed. However, it was later on noted that a sub-linear function ($\propto \sqrt{r}$) on r was returned in fact a better fit of experimental data without critically affecting the complexity of the model. This hypothesis also matched the considerations on rapidly increasing [decreasing] of $\beta(r)$ [$\nu(r)$] in R2 regimes and then a linear trend with increasing $r \in R3$.

Comment on gridsearch and purpose of this investigation Note that, although a $\beta(r = 0) \neq 0$ would have been intuitively more reasonable choice, the rough grid search performed returned a better approximation of the data when zero or close to zero values for $\beta(r)_{min}$ were used.
This features suggests a potential fallacy of the present analysis: on the one hand, due to the large amount of parameters ($\omega_0, \omega_1, \beta_0, \beta_1, \mu, \nu_0, \nu_1, \theta_1, s_1$), lot of effort (although needed for more thorough analysis) would have been needed in order to perform a higher resolution grid search and return more fitting results. On the other hand, allowing for a better tuning of the parameters in order to match MODIS data would have most probably result in overfitting for this specific dataset, returning no general knowledge on the model itself.

Therefore, it was preferred still to have a *rough* fit of CME analysis on the experimental data, without looking for fine tuning of the parameters and with the goal of providing a solid enough proof of principle. Still it is possible to obtain better results just tuning in the parameters more finely, though it is unsure whether that could be meaningful without any different dataset to validate the simulations with. Additionally, it is to be recalled that the present sets of parameters found are most likely to be valid only in the specific rainfall ranges considered.

3.3 Code

The core part of the `MATLAB` code used for the implementation of the CME algorithm following from Eq.3 is in List.1. `ode113` MATLAB function was used for the time integration using `relative tolerance` of $\mathcal{O}(10^{-15})$ and `absolute tolerance` of $\mathcal{O}(10^{-100})$. A grid search allowed for finding out relevant ranges of parameters to probe and determining crucial sets of parameters that returned results of the CME comparable with experimental data output.
The CME `MATLAB`code, together with the one solving the ODE and a `Python` script for the

post processing and analysis was organized in a consistent workflow in order to allow efficient parameter search and data exploration from the outputs.

```
E_1   = sparse( diag( ones( N, 1 ), -1 ));
Em1   = sparse( diag( ones( N, 1 ),  1 ));

T01 = kron( eye(N+1), E_1 );
T10 = kron( E_1, eye(N+1) );
T0m1 = kron( eye(N+1), Em1 );
Tm10 = kron( Em1, eye(N+1) );

I  =  sparse( 1:(N+1)^2, 1:(N+1)^2, 1 );

TWx1   = sparse( 1:(N+1)^2, 1:(N+1)^2, X );          %Grass
TWx2   = sparse( 1:(N+1)^2, 1:(N+1)^2, Y );          %Tree
TWx3   = sparse( 1:(N+1)^2, 1:(N+1)^2, (N+1)-X-Y);   %Savanna
TWx3(TWx3 < 0) = 0;

%%Parameters (example, Touboul parameters)
omega_1 = .2;
omega_0 = .9;
mu = .2;
nu = .1;
s_1 = .01*(N+1);
theta_1 = .4*(N+1);

omega_G = I*omega_0 + I*(omega_1-omega_0).*... %tanh!
    ( exp(2*(TWx1-I*theta_1)/I*s1)-I*1)./...
    ( exp(2*(TWx1-I*theta_1)/I*s1)+I*1);

%%Reactions:

%R1 (G,T)->(G+1,T) @ mu*(N+1-G-T)
R1 = mu*(T10-I)*TWx3;
%BC: if G=N, no R1 can take place
for i = (N+1)^2-N:(N+1)^2
    R1(i,i)=0;
end

%R2 (G,T)->(G+1,T-1) @ nu*T
R2 = nu*((T10*T0m1-I))*TWx2;
%BC: if G=N or T=0, no R2 can take place
for i = (N+1)^2-N:(N+1)^2
    R2(i,i)=0;
end
for i = 1:N+1:(N+1)^2
    R2(i,i)=0;
end

```

```
%R3 (G,T)->(G-1,T) @ beta*G*T
R3 = (Tm10-I)*beta*(TWx1*TWx2);
%BC: if G=0, no R3 in G can take place
for i = 1:N+1
    R3(i,i)=0;
end

%R4 (G,T)->(G,T+1) @ omega_G*(N+1-G-T)
R4 = (T01-I)*(omega_G)*TWx3;
%BC: if T=N, no R4 can take place
for i = N+1:N+1:(N+1)^2
    R4(i,i)=0;
end

J = R1+R2+R3/(N+1)+R4;
```

Listing 1: Matlab Jacobian matrix (J) implementation for the CME algorithm

In preliminary simulations, the only exit condition used for the simulation was a limit at about $t_{end} \sim 10^6$ for the time integration. In these runs, the expected value of $G(t)$ and its variance were monitored in order to validate that the system indeed converged towards and equilibrium.
This knowledge was used for subsequent runs in which, in order to have faster computations and still reliable enough results, an additional exit condition was added later on: the run was ended before hitting t_{end} if, *for each* cell in the phase space, the difference between values two consecutive time integration was less than 10^{-20}. This choice was motivated by the fact that it was verified numerically that configurations rapidly ($t < 10^3$) converged to an equilibrium for the given parameters chosen.

CME simulation code In the attached files, two MATLAB codes will be provided.The core idea for the following codes were based on suggestions from dr. Ivan Kryven.

The *savanna_CME.m* code was used for simulating the CME for given initial conditions and parameters. This script was then included in a loop for sweeping over different initial conditions and a Python script was later used for analyzing the result. This script automatically creates/cleans up the folders and save to the appropriate path the raw data from the CME over time and in the final state. This setup is needed in order to easily relate MATLAB results with the Python script in the workflow.

The *OutputAndPlot.m* code was used for checking the progresses of the simulation during the run and displays the values the PDF in the grid. In the contour plot displayed, every adjacent line separates region differing in the PDF values by one order of magnitude, starting from a minimum value of 10^{-15}.

Part II

Results

3.4 Chosen parameters

Four candidate sets of parameters were chosen as representative of different outcomes for the comparison of MODIS data with simulations. The chosen parameters are in Tab.2. Simulations for different parameters were launched for different initial conditions and, for each set of parameters and initial conditions, both ODE and CME approaches were used: this helped identifying the main advantages and disadvantages of each that will be discussed in this section.

It will be shown that only *Set1* and *Set4* parameters were able indeed to return a CME partially matching the MODIS data. Due to the non-linear model in Eq.3, it was however hard to pinpoint exactly which of the parameters most dramatically affected the simulation output, especially considering that it was not possible to have any preliminary analytical clue, made exception for trivial cases. The complexity of the phase space in dependence of (constant) model parameters is depicted in [3]-Fig.1.
As it will be shown in the following plots, ODE and CME often returned not matching results and therefore it was unfeasible to preliminarily probing what the outcome of the CME simulation would have been just by using the ODE approach.This also means that the analysis in literature [3] can only provide a partial intuition for the values of the ranges of parameters that will yield to a particular phase portrait.

Parameter	**Set1**	**Set2**	**Set3**	**Set4**
ω_0	.5	.5	.55	.5
ω_1	.1	.2	.2	.1
β_0	0	0	0	0
β_1	5	5	5	5
μ	.1	.6	.4	.2
ν_0	.4	.3	.9	.2
ν_1	.6	.8	.5	.8
θ_1	.3	.4	.4	.4
s_1	.03	.05	.01	.05

Table 2: Sets of parameters used in CME and ODE for comparison with experimental data from [5].

For all the simulations here presented, it was chosen a gaussian profile for the PDF with size of the grid of `N`= 50 and standard deviations $\sigma_{G_0} = \sigma_{S_0} = N/10$. Different sets of

initial mean values for each set of parameters were simulated,:

$$[G_0, S_0] = \mathbb{N} \cdot \begin{cases} [.8, .2] \\ [.8, .0] \\ [.2, .8] \\ [.2, .0] \\ [.0, .2] \\ [.0, .8] \end{cases} \tag{7}$$

Results from the same set of parameters will be presented only when significant differences between runs with same parameter and different initial conditions will be found.

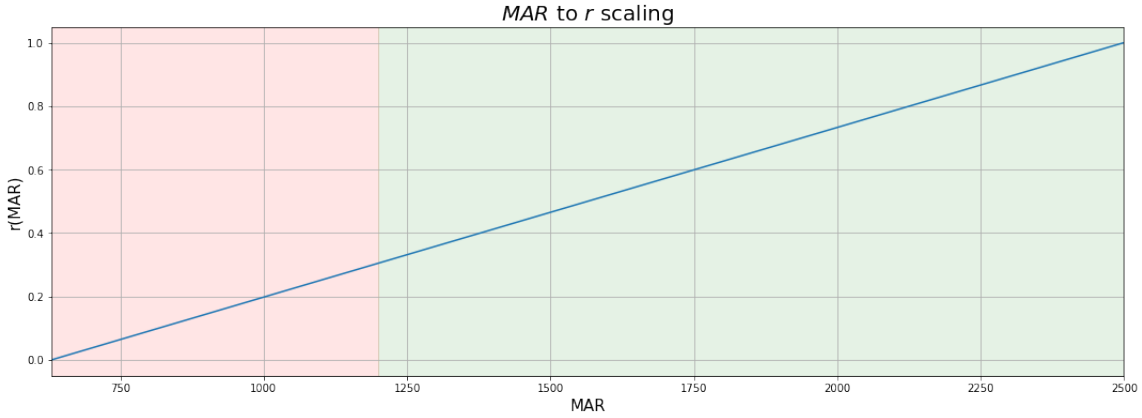

Figure 9: MAR to r scaling. As previously shown, the red region refers to the R2 regime ($MAR \in [630 - 1200]$) while the green regions is representative of the R3 regime ($MAR \in [1200 - 2500]$). For future reference, the separation between R2 and R3 occurrs at $r \sim .33$

3.5 Comparison with MODIS data

In order to perform a solid enough comparison between results from CME and MODIS data, it was chosen to organize MODIS data in a 2D histogram and to compare expected values from MODIS data withe expected values from CME. By doing so, scaled MODIS data were organized in bins of $\sim 95 \frac{mm}{year}$: this allowed to keep a high enough resolution while preserving the global trend in non-tree-coverage. Data along each r value was then normalized in order to allow for a direct comparison with the CME results. It will be shown that, for the chosen sets of parameters, CME simulations seem to better fit the global behaviour of the experimental data when compared with ODE results.
An example of the output from this analysis is given in Fig.10-11.

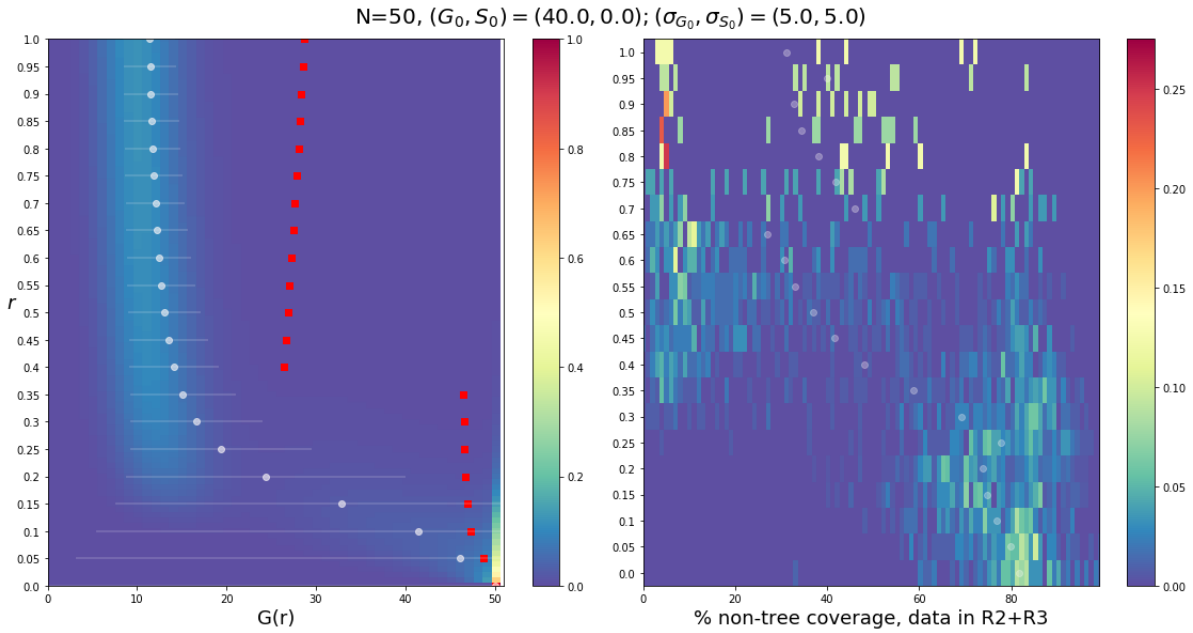

Figure 10: Example of comparison of results. *Set4* parameters in Tab2. Left: ODE (red dots), CME PDF (heatmap) and expectation values with standard deviation (gray dots); Right: 2D histogram of MODIS data, bin size $\sim 95\frac{mm}{y}$, grey points represent the expected values from the normalized bin along the y-axis.

Stability over different initial conditions Fig.10-12-13 suggest that little to none significant differences between runs with same parameters and different initial conditions could be observed with the chosen parameters for CME. Therefore, results for different initial conditions will be shown here only if significantly differing from one another.
If on the one hand the CME results only show little differences over different initial conditions, on the other hand ODE results are significantly dependent on initial conditions as anticipated in Fig.7 where constant parameters were used.
This feature was expected to be more pronounced in the CME analysis while it turned out to be mostly absent. This could be due to the intrinsic dynamic of the CME or to the large initial PDF dispersion used.

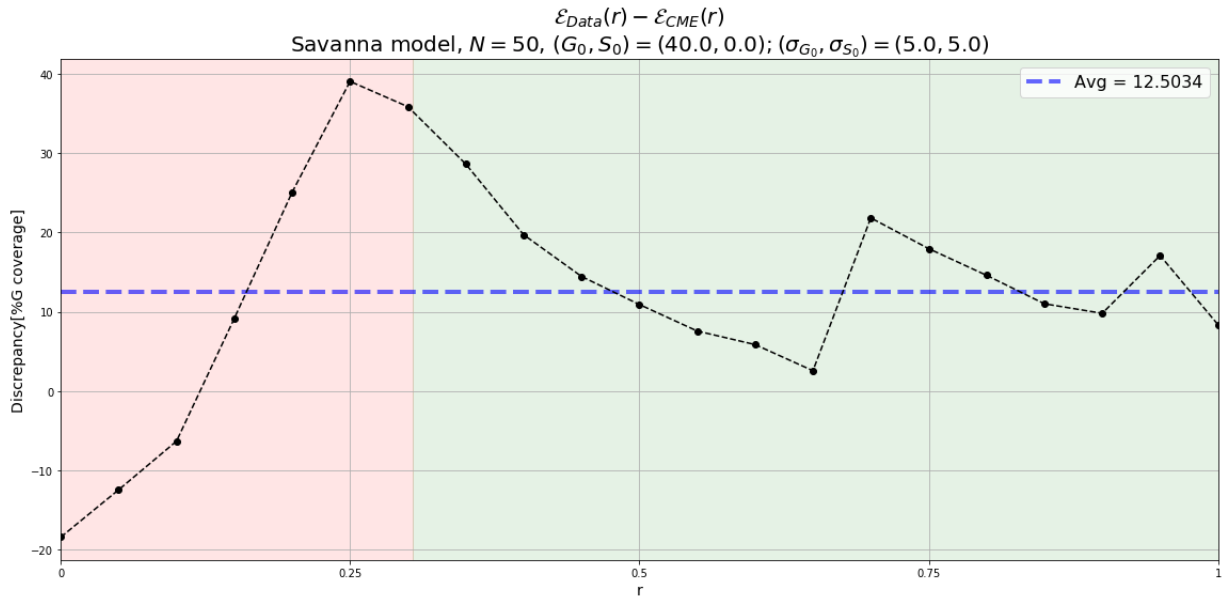

Figure 11: *Set4* parameters in Tab2. Comparison of expected value from CME and MODIS data for correspondent values of r. It can be seen that better agreement is found for higher MAR regimes. This could also be due to the higher standard deviation of CME data for lower r. A similar outline was obtained for all other initial conditions used for this set of parameters and therefore results for discrepancy of expected values are not going to be presented again.

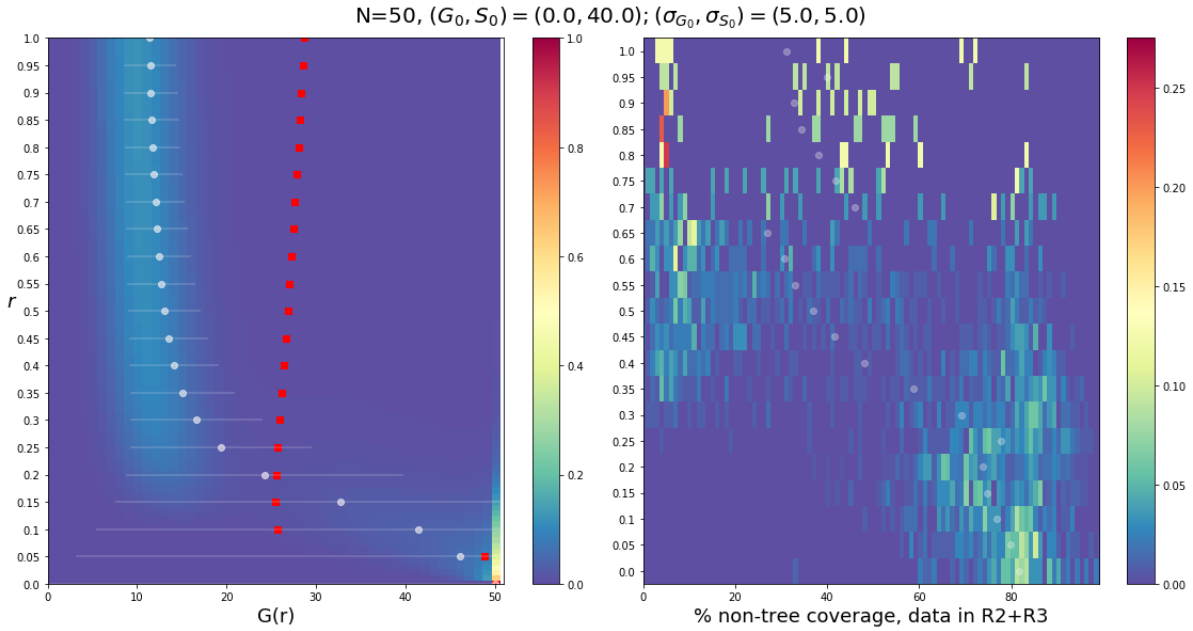

Figure 12: *Set4* parameters in Tab2. Left: ODE (red dots) and CME PDF (heatmap) and expectation values with standard deviation (gray dots); Right: 2D histogram of MODIS data, bin size $\sim 95\frac{mm}{y}$, grey points represent the expected values from the normalized bin along the y-axis.

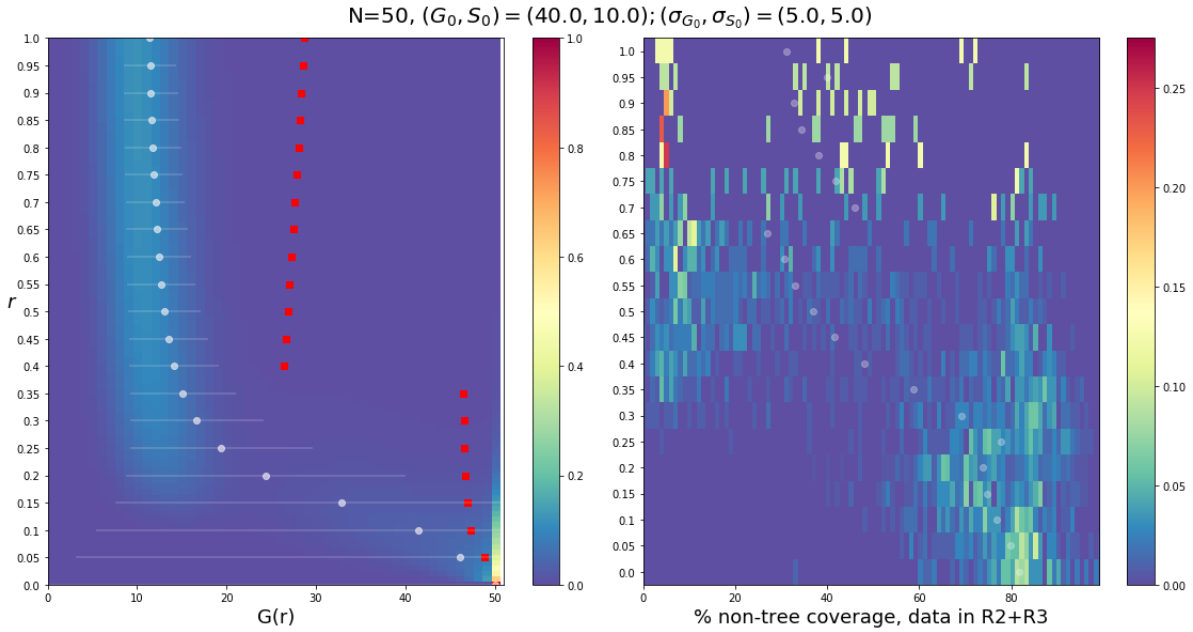

Figure 13: *Set4* parameters in Tab2. Left: ODE (red dots) and CME PDF (heatmap) and expectation values with standard deviation (gray dots); Right: 2D histogram of MODIS data, bin size $\sim 95\frac{mm}{y}$, grey points represent the expected values from the normalized bin along the y-axis.

3.6 Result: *Set1* parameters

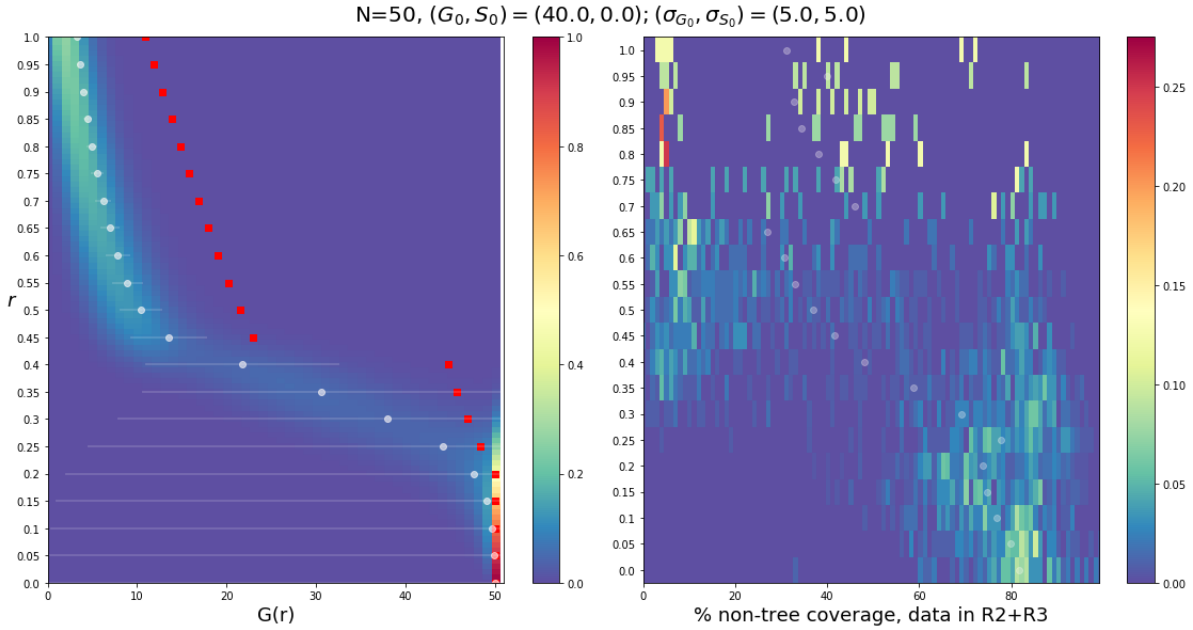

Figure 14: Example of comparison of results. *Set1* parameters in Tab2. Left: ODE (red dots) and CME PDF (heatmap) and expectation values with standard deviation (gray dots); Right: 2D histogram of MODIS data, bin size $\sim 95\frac{mm}{y}$, grey points represent the expected values from the normalized bin along the y-axis.

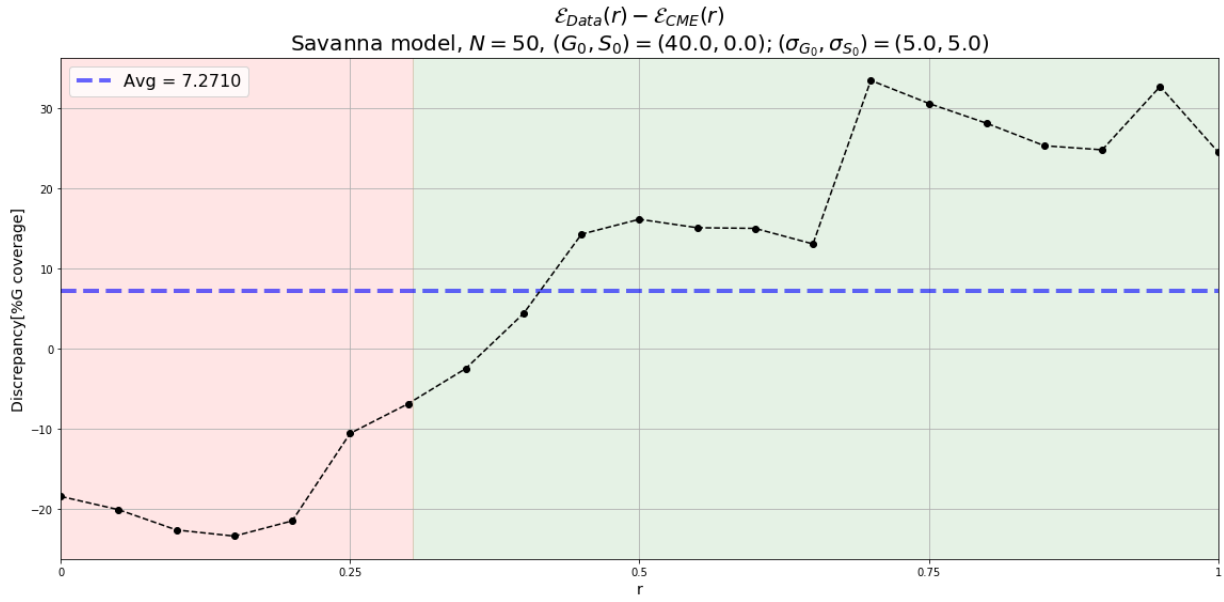

Figure 15: *Set1* parameters in Tab2. Comparison of expected value from CME and MODIS data for correspondent values of r.

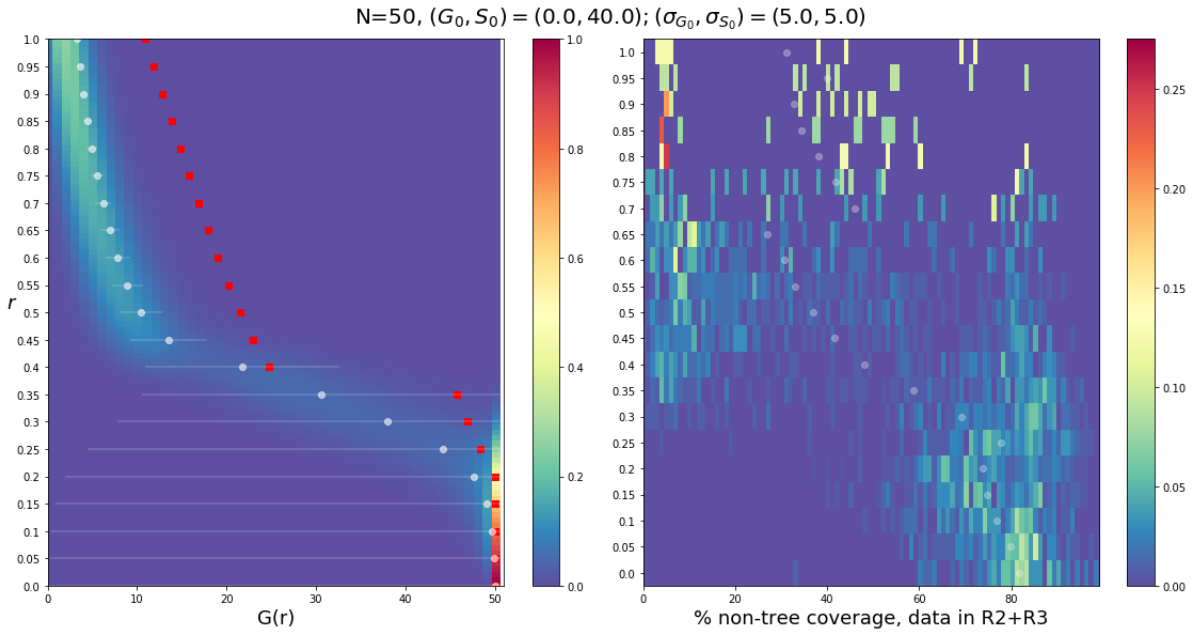

Figure 16: *Set1* parameters in Tab2. Left: ODE (red dots) and CME PDF (heatmap) and expectation values with standard deviation (gray dots); Right: 2D histogram of MODIS data, bin size $\sim 95\frac{mm}{y}$, grey points represent the expected values from the normalized bin along the y-axis.

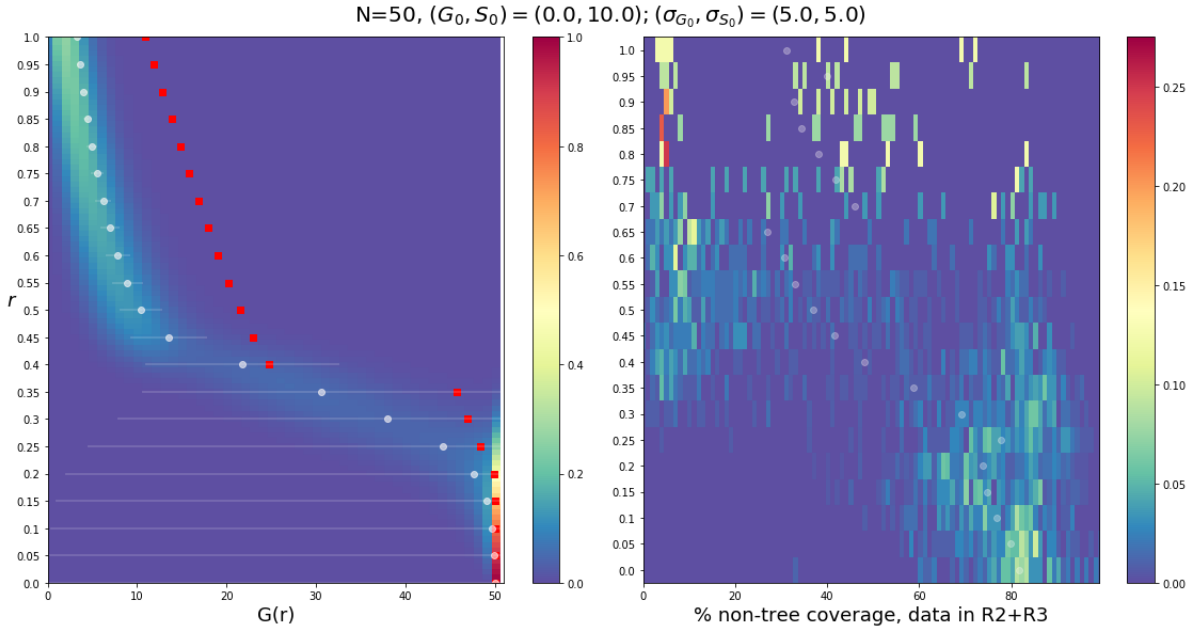

Figure 17: *Set1* parameters in Tab2. Left: ODE (red dots) and CME PDF (heatmap) and expectation values with standard deviation (gray dots); Right: 2D histogram of MODIS data, bin size $\sim 95\frac{mm}{y}$, grey points represent the expected values from the normalized bin along the y-axis.

3.7 Result: *Set2* parameters

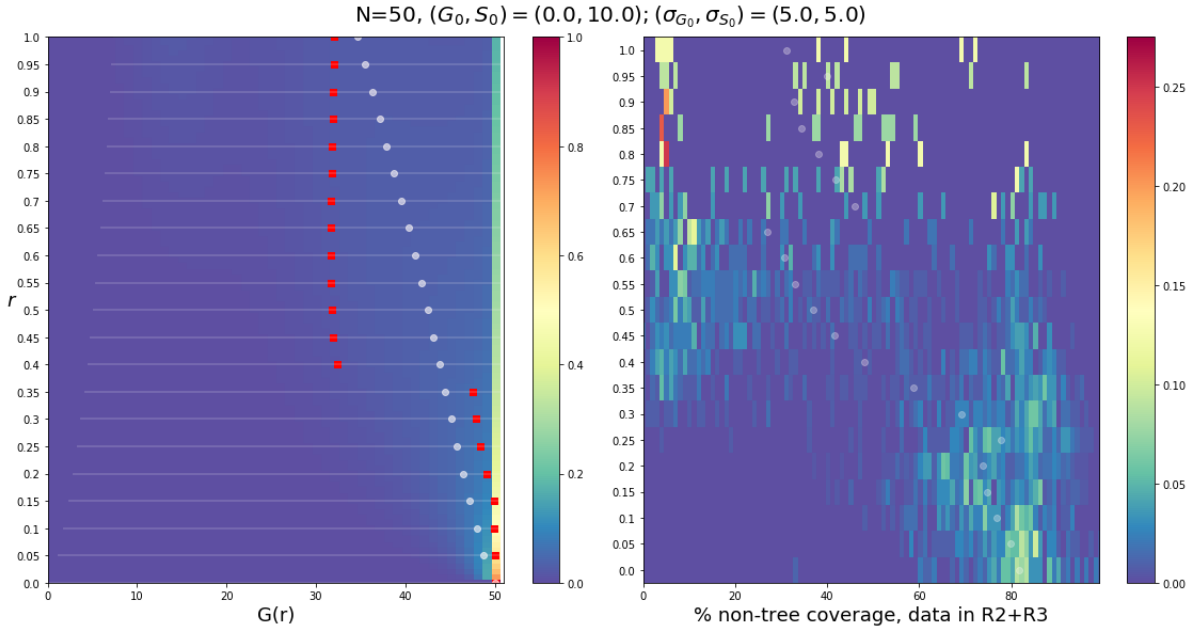

Figure 18: Example of comparison of results. *Set2* parameters in Tab2. Left: ODE (red dots) and CME PDF (heatmap) and expectation values with standard deviation (gray dots); Right: 2D histogram of MODIS data, bin size $\sim 95\frac{mm}{y}$, grey points represent the expected values from the normalized bin along the y-axis.

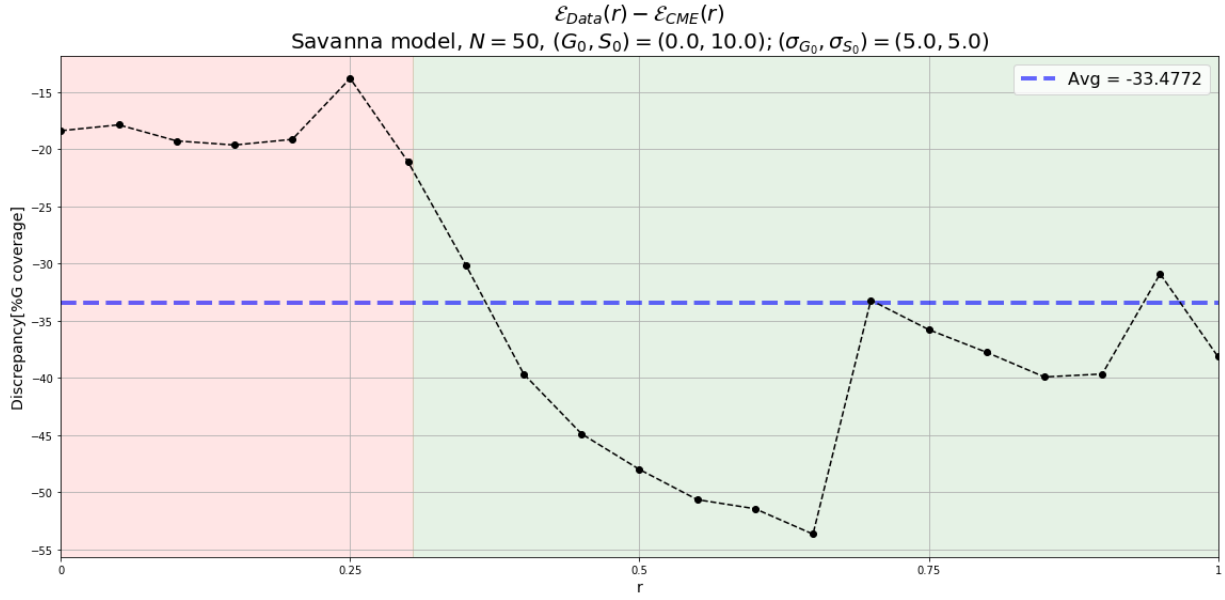

Figure 19: *Set2* parameters in Tab2. Comparison of expected value from CME and MODIS data for correspondent values of r.

3.8 Result: *Set3* parameters

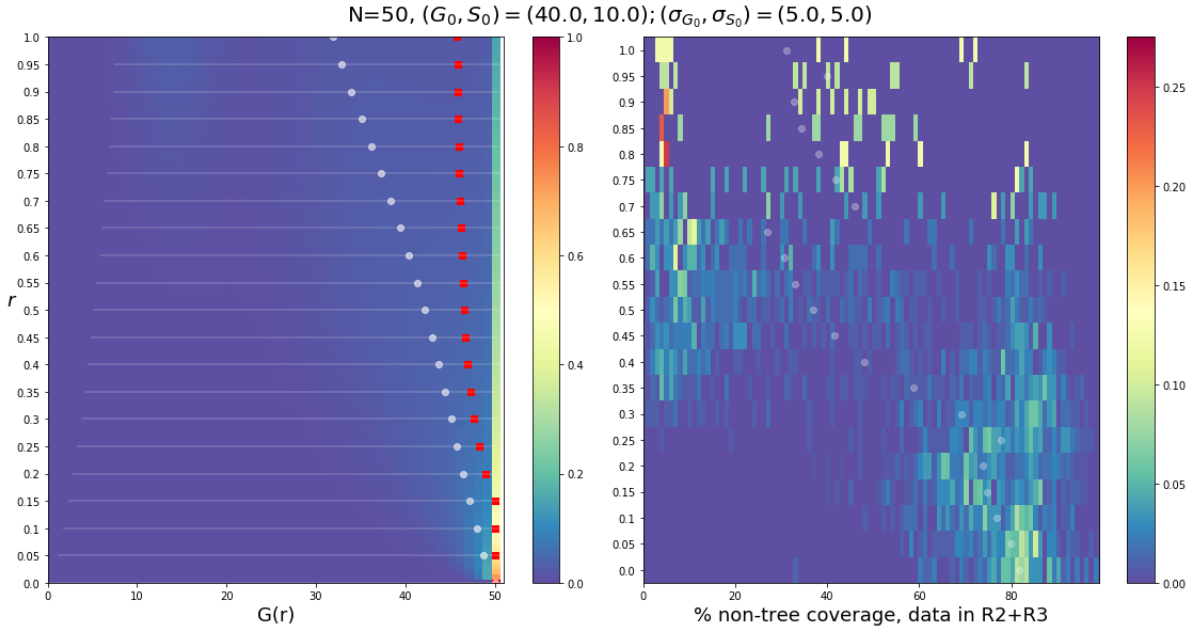

Figure 20: Example of comparison of results. *Set3* parameters in Tab2. Left: ODE (red dots) and CME PDF (heatmap) and expectation values with standard deviation (gray dots); Right: 2D histogram of MODIS data, bin size $\sim 95\frac{mm}{y}$, grey points represent the expected values from the normalized bin along the y-axis.

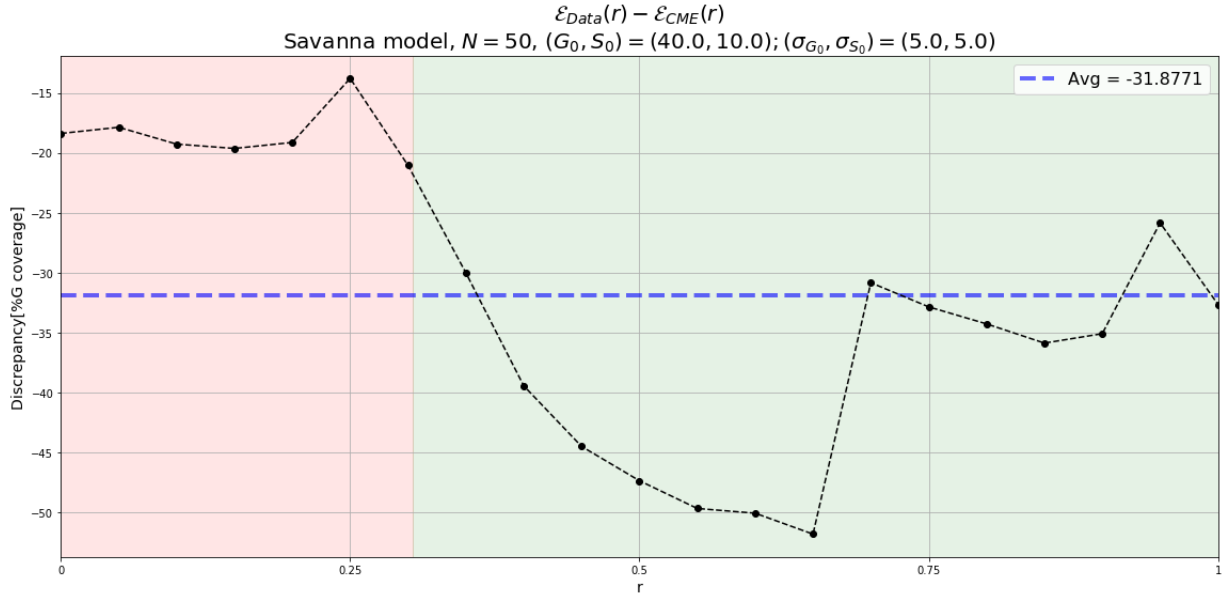

Figure 21: *Set3* parameters in Tab2. Comparison of expected value from CME and MODIS data for correspondent values of r.

3.9 About parameter tuning

The relevant features that emerge from the presented outputs can mostly fall into two main categories: those deriving from the actual dynamic of the model and the ones which emerge CME method exploited in this work.
Nevertheless, it is often unclear if a sharp separation between these two can be traced at all in these results: this is mostly due to the fact that Staver model chosen for interpreting the MODIS data with CME has quite a complex phase space when the different (non constant) parameters are considered. This dramatically affects the complexity in interpretation of both analytical analyses with standard methods and any further direct investigation over new methods for modelling such data.
Consequently, this means that CME simulation is needed to validate *simultaneously* model and method while little can be said about the two separately when comparing with experimental data.

Results here reported represents two examples of parameter sets which returned plausible matching with experimental data (*Set1* and *Set4* as shown in Figs.10-11-14-15) and no match with MODIS observations (*Set2* and *Set3* as shown in Figs.18-19-20-21. The two couples of good and bad parameters can be used as starting points for further search in the parameter space.

From the simulation run in this work, it seems that *Set1* returned partially good results as for differences of expected values (Fig.15).

Please note that the ODE behaviour for *Set4* greatly differs from CME trend and MODIS data while there is some partial agreement between ODE and CME results for *Set1*. This supports the hypothesis that it not possible to rely on an initial exploration of the solutions using an ODE approach before running the CME simulations as the two approaches indeed return different results. This last feature is present, though less pronounced, between simulations with *Set2* and *Set3* parameters sets where the discrepancies of expected values are even way larger.
In addition to that, note that for low r the CME returned dispersed results over $G(r)$ and the error bars greatly increased with lower r: it is therefore impossible to clearly state validate the advantages of one approach over the other for low r, although the expected values from CME seems still to interpret sufficiently well the experimental data a bit better, especially for what concerns the transcritical phase transition threshold. This last point holds true in particular for *Set1* which yielded the best matching results with MODIS data.

Part III

Conclusions and outline

MODIS data of distribution of grass, saplings and trees in savanna biomes for different rainfall regimes have been investigated using savanna Staver model [4]. First, Staver model was first rephrased in terms of **C**hemical **M**aster **E**quation (CME) [1]. Secondly, the parameters in the workflow of CME were tuned in order to match experimental observations: this eventually allowed to infer a possible range of parameters for Staver model that approximately fitted the MODIS data.

This work highlighted several peculiar features of the CME algorithm over a canonical ODE analysis for this specific benchmark and helped in outlining a starting point for using CME approach in such and similar models as a method for inferring model parameters using (e.g.) maximum likelihood methods.

It is to be stressed out that the obtained set of parameters actually fit Staver model only when CME is considered (compare Fig.13 and Fig.14) and therefore it is actually non trivial to determine beforehand if the CME simulation will return reliable results just based on the ODE analysis.

Some parameters yielded a better agreement for higher rainfall regimes(*Set4* data in Fig.11) while others (*Set1*) matched experimental observation in lower rainfall regimes. This may suggest that CME analysis can return a reliable method for inferring model parameters of Staver model only for specific rainfall regimes: a narrower validity region in this case would suggest either that changing sets of parameters must be considered over the different rainfall regimes (e.g. using a combination of *Set1* in R2 and *Set4* in R3 would seem a good tradeoff) or that Staver model need to be further adapted to CME dynamics in order to obtain matching results.

The present work allowed helped to highlight some of the unique traits of the CME method: some of them such as the possibility to describe the dynamics of small systems and the possibility to detect and accurately locate bistabilities region boundaries, were already explored in prior case of study (using CME on SIS, SIR model); others emerged during the present work, such as the fact that CME method is more suitable when the phase portrait for the model is complex and uncertainties about the initial conditions can dramatically affect the actual evolution over time of the system.
Another possibility for example, not explored for this case of study, would have been to have a comparative analysis between Stochastic Simulated Algorithms (SSA) and CME results for the same set of parameters and checking which of the two actually yielded a

better approximation of the experimental data.
Please note that results obtained were meant to approximate the specific dataset available and therefore overfitting and confirmation bias cannot be excluded in the parameter search process.

The work here presented focused on how some of these peculiar features can help in the interpretation of real data: this framework, together with the organized workflow canvas, can lend itself as a starting point for further analyses, especially for what concerns translating ODE models in the CME paradigm and/or a more detailed grid search of the parameters for the Savanna model here investigated and others.

An interesting research question, considering all the peculiar features and issues related to the CME approach here presented, would be to check whether it is possible, given an experimental PDF, to fist start directly looking for a CME model like the one in Eq.3 starting from the simplest combination of all the possible reactions that can occur. Then, it would be interesting to find a way to rephrase back the CME obtained into an ODE system for model validation. Even if with larger initial computational costs in the reactions/parameters search, this *reversed* procedure may help in determining unknown models for experimental PDF and/or having an alternative validation of the model and stems directly from the actual data.

References

[1] Higham, 2008; *Modeling and Simulating Chemical Reactions*, Society for Industrial and Applied Mathematics. Vol. 50, No. 2, pp. 347–368.
`https://doi.org/10.1137/060666457`

[2] Beckage et al., 2006; *Vegetation, Fire, and Feedbacks: A Disturbance-Mediated Model of Savannas*, Am Nat. 2009 Dec;174(6):805-18. doi: 10.1086/648458.
`https://www.ncbi.nlm.nih.gov/pubmed/19860540`

[3] Touboul et al., 2017; *On the complex dynamics of savanna landscapes*, E1336–E1345 — PNAS — Published online January 29, 2018.
`http://www.pnas.org/cgi/doi/10.1073/pnas.1712356115`

[4] Staver et al., 2011; *Tree cover in sub-Saharan Africa: Rainfall and fire constrain forest and savanna as alternative stable states*, Ecology, 92(5), 2011, pp. 1063–1072.
`https://doi.org/10.1890/10-1684.1`

[5] D'Onofrio et al., 2018; *Not only trees: Grasses determine African tropical biome distributions via water limitation and fire*, Global Ecol Biogeogr. 2018;27:714–725.
`https://doi.org/10.1111/geb.12735`

[6] Lee et al. 2007, *Nonlinear Dimensionality Reduction*, Springer, New York, NY
https://link.springer.com/book/10.1007/978-0-387-39351-3